J. Fluid Mech. (1996), vol. 315, pp. 267–291

Oscillations of a moderately underexpanded choked jet impinging upon a flat plate

By CHIH-YU KUO AND ANN P. DOWLING

Cambridge University Engineering Department,
Trumpington Street, Cambridge CB2 1PZ, UK

(Received 13 July 1995 and in revised form 22 January 1996)

The oscillation of a moderately underexpanded choked jet impinging upon a flat plate is investigated both analytically and numerically. The feedback mechanism between oscillations of the standoff-shock and the plate is clarified. Pressure waves produced by the motion of the shock are reflected by the plate. In addition, oscillations in the shock position lead to downstream entropy fluctuations, which generate pressure waves as they are convected through the stagnation flow near the plate. A linear stability analysis is used to investigate the stability threshold and frequencies of oscillation, as a function of jet pressure ratio and nozzle-to-plate distance. The analytical predictions are compared to results from a numerical simulation and to the experimental data of Powell (1988) and Mørch (1963, 1964).

1. Introduction

Sound generation by jets impinging upon various solid obstacles has been studied for a long time (see, for example, Hartmann & Trolle 1927; Hartmann 1939; Chanaud & Powell 1963; Rockwell & Naudascher 1979) and it is well established that acoustic or hydrodynamic feedback can lead to self-excited oscillations at discrete-frequencies. Powell (1988) and Henderson & Powell (1993) report an extensive experimental investigation of the discrete frequency sound produced by underexpanded choked jets impinging on plane surfaces. This jet oscillation and the emitted sound is of practical importance for rocket exhausts at launch and for the jets from vertical-takeoff-and-landing aircraft. Our motivation for studying this topic arises from the potential use of these discrete frequencies in metrological applications (V. M. Weerasinghe & L. S. Chung 1993, personal communication) to determine and control the height of a machine tool above a workpiece.

We are interested in sound generated by moderately underexpanded jets impinging on flat surfaces. The jet emerges choked from a convergent nozzle, with a total pressure p_0 at least a factor 1.89 larger than the ambient pressure p_a. This overpressure results in the famous shock cell structures of the jet. For p_0/p_a between about 2.5 and 3.8, the jet is referred to as 'moderately underexpanded'. In this range, a weak near-conical shock wave is formed at the end of each cell due to the merging of compressive waves reflected from the jet boundary. This shock is referred to the free jet shock. The impingement of this jet normally onto a flat plate located in the first few shock cells leads to the formation of a well-defined standoff shock wave upstream of the plate. Across the standoff shock, the jet suddenly decelerates to subsonic flow and is then deflected by the plate. This subsonic flow region downstream of the shock will be referred to the stagnation flow region.

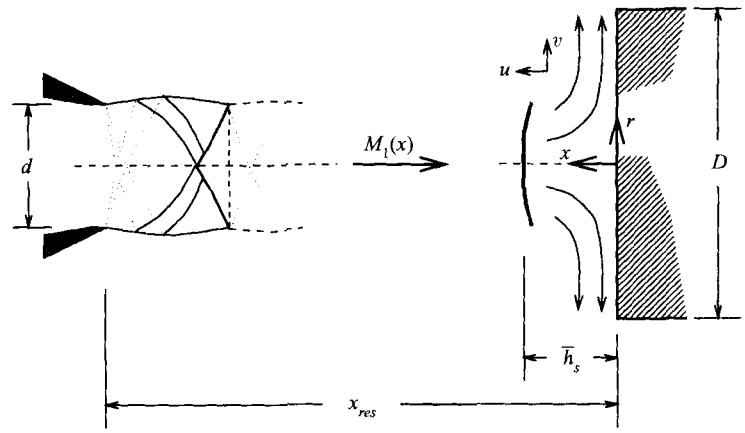

FIGURE 1. Flow pattern and coordinate system. From §2.5 onwards, lengths are non-dimensionalized with respect to the nozzle diameter, i.e. $d = 1$.

The discharge flow then accelerates along the surface of the plate and regains its supersonic speed beyond the 'sonic point'. A sketch of the mean flow field is shown in figure 1.

The experimental investigations by Powell (1988) and Henderson & Powell (1993) reveal two important sources of discrete-frequency perturbations in the jet–plate geometry. These are standoff shock oscillation and vortex shedding in the jet shear layer. Both self-excited oscillations rely on acoustic feedback to sustain the motion. The vortex shedding mechanism involves jet disturbances excited at the nozzle exit and acoustic feedback between the plate and the nozzle lip (Powell 1988). This self-excited oscillation occurs even for subsonic jets (Tam & Ahuja 1990; Ho & Nosseir 1981). In this paper, our major concern is the instability associated with the standoff shock oscillation. Powell (1988) and Henderson & Powell (1993) observe and clarify several characteristics of the resultant flow disturbances. Large self-excited shock oscillations are found when the standoff shock lies in the downstream portion of each free jet shock cell. The schlieren photographs show flow perturbations to be axisymmetric. The main feedback loop in this mechanism involves sound waves reflected between the plate and the standoff shock and this influences the frequency of the oscillation. However, Henderson & Powell (1993) point out that, at least for some flow conditions, some feedback to the nozzle is also required if the oscillation is to be self-sustaining. The shock oscillation sound is found to dominate the vortex shedding sound when the plate size is less than two jet diameters. Similar self-excited oscillations involving shock motion occur when the jet blows onto a closed tube (Hartmann & Trolle 1927). Discrete-frequency tones are also emitted from oscillations of the shock structure of very highly expanded supersonic impinging jets (see Glaznev 1977; Glaznev, Demin & Yakushev 1977).

Mørch (1964) investigates the shock motion both theoretically and experimentally. His theory concentrates on the flow near the central axis which is crucial in the feedback mechanism. He approximates the mean flow downstream of the shock by an incompressible stagnation flow and investigates the propagation of pressure waves generated at the shock through this region and their reflection at the plane surface. However, according to this theory, linear flow disturbances are always stable and decay exponentially with time. The self-excited shock oscillations observed experimentally are not predicted. We believe that an important mechanism is omitted from Mørch's

theory. Oscillations in the shock position lead to downstream entropy fluctuations. As these entropy perturbations or 'hot-spots' are convected through the stagnation flow near the plate, they generate additional pressure waves which can propagate upstream and interact with the shock. In §2, we extend Mørch's analysis to include these entropy disturbances as acoustic source terms. We use the extension of Howe (1975) to Lighthill's acoustic analogy. In Howe's formulation, stagnation enthalpy is used as the independent variable and this highlights inhomogeneous entropy disturbances as acoustic sources. We include the effect of the entropy disturbances and determine the eigenfrequencies as complex solutions of a characteristic equation of linear stability theory. Our linear stability theory requires the mean flow field to be specified. We use a numerical simulation described in §3 to obtain the required details of the mean flow and to test the approximations made in the linear theory. The numerical simulation is unsteady and by taking the Fourier transform of the flow variables, we can determine the frequency of oscillation. In §4, the frequencies predicted by the linearized theory and by the numerical simulation are compared with the experimental data of Powell (1988) and Mørch (1963, 1964). The agreement is encouraging.

2. Linear stability theory

2.1. *Mean flow*

A moderately underexpanded jet emerges from a nozzle of diameter d and impinges on a flat plate. The flow is axisymmetric. Following Mørch's model, we assume that the main contribution to the feedback is from the region near the jet axis, while the shock undergoes a small oscillation in the axial direction. Therefore, the standoff shock will be assumed to be normal to the axis at a distance $h_s(t)$ from the plate and to divide the flow into an upstream supersonic jet and a downstream stagnation flow.

We choose the coordinate system shown in figure 1. The analytical work is for an infinitely large plate $D = \infty$. The origin is on the plate, with the positive x-axis towards the direction of the incoming flow. The overbar denotes the mean of a flow variable evaluated at a fixed position and subscripts 1 and 2 represent quantities upstream and downstream of the shock respectively.

The supersonic flow upstream of the standoff shock is uninfluenced by downstream perturbations. The Mach number near the central axis depends only on the non-dimensional axial distance from the nozzle lip and on the jet pressure ratio p_0/p_a. It can be obtained either by experimental measurement or by a straightforward numerical calculation of a steady free jet. Figure 2 shows the variation of Mach number along the central axis of a free jet, for $p_0/p_a = 3.72$, calculated by the method of characteristics and by the numerical simulation described in §3. Results from the two methods are in good agreement and fit the schlieren photographs in Hartmann (1939) and Powell (1988). A weak nearly conical free jet shock can be seen near the end of the first cell, $1.15d$ from the nozzle. There is negligible entropy variation across this weak shock in agreement with the experimental results of Hartmann (1939, figure v.9b). The Mach number decrease in the second cell is more gradual, which is supported by Powell's (1988, figure 3c) optical observation of the free jet. However, this smoothing may have been exaggerated by numerical dissipation.

As in Mørch's approach, we assume that the Mach number just upstream of the standoff shock is high enough to result in a strong shock and a low downstream Mach number ($\bar{M}_2^2 \ll 1$). Then, the mean stagnation flow downstream of the normal

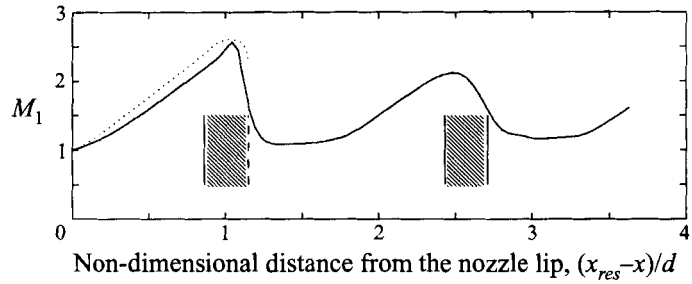

FIGURE 2. Variation of Mach number along the central axis of a free jet for $p_0/p_a = 3.72$: —, calculated by the numerical simulation described in §3; ···, calculated by the method of characteristics; — — —, the position of the free jet shock calculated by the method of characteristics; ▒, unstable standoff shock locations calculated in §2.6.

standoff shock can be assumed to be nearly incompressible. The mean entropy $\bar{S}_2$, temperature $\bar{T}_2$, and sound speed $\bar{c}_2$ can be regarded as uniform since they have only negligible $O(\bar{M}_2^2)$ spatial variations based on the isentropic relations in this region.

This downstream incompressible mean flow can be approximated by an irrotational incompressible stagnation flow (Mørch 1964), which gives $\bar{u}_2 = -\alpha x, \bar{v}_2 = \frac{1}{2}\alpha r$, and the velocity potential

$$\bar{\phi}_2 = \tfrac{1}{4}\alpha(r^2 - 2x^2). \tag{2.1}$$

The mean flow velocity just downstream of the shock, $\bar{u}_2(\bar{h}_s)$, whose mean position is at $x = \bar{h}_s$, is given by the Rankine–Hugoniot relations (see §2.2); α then follows from $\bar{u}_2(\bar{h}_s) = -\alpha\bar{h}_s$. The numerical simulation described in §3 shows that (2.1) is a reasonable approximation to the flow provided the mean shock position is within $0.6d$ of the plate. As discussed in §3, for larger values of $\bar{h}_s$, a recirculation bubble may form near the plate (Kalghatgi & Hunt 1976). A typical numerically calculated flow field is shown in figure 7.

2.2. *Oscillating normal shock*

To ensure a causal response and to avoid any ambiguity in the choice of the appropriate branch cuts, we assume that the oscillation of the standoff shock starts at a fixed time T_0. Subsequently, it undergoes a small harmonic oscillation of complex eigenfrequency ω. Our aim is to determine the eigenfrequencies ω for which the boundary conditions across the shock and on the plate are satisfied. The shock position can therefore be expressed as

$$h_s(t) = \bar{h}_s + l e^{i\omega(t-T_0)} H(t - T_0)$$

where $\bar{h}_s$ is the mean shock position, l is the small initial amplitude and H denotes the Heaviside function. In order to be able to apply the Rankine–Hugoniot relations in their usual form, we define Mach numbers at the shock to be positive. Hence, M_1, the Mach number just upstream of the shock is related to u_1, the local fluid velocity in the x-direction, by $M_1 = -u_1/c_1$, where c_1 is the local speed of sound. For linear shock displacements, we can expand

$$\begin{aligned} M_1(h_s) &\approx M_1(\bar{h}_s) + \frac{\mathrm{d}M_1}{\mathrm{d}x}(\bar{h}_s) l e^{i\omega(t-T_0)} H(t - T_0) \\ &= \bar{M}_1 + \frac{\mathrm{d}\bar{M}_1}{\mathrm{d}x} l e^{i\omega(t-T_0)} H(t - T_0), \end{aligned}$$

where higher-order terms of l have been neglected. Other flow variables, e.g. sound speed c_1, can be expanded in a similar way.

The Rankine–Hugoniot relations across the normal shock are to be applied in a frame of reference in which the shock is stationary. In this frame:

$$M_{1,sh} = M_1 + \frac{1}{c_1}\frac{\mathrm{d}h_s}{\mathrm{d}t} \approx \bar{M}_1 + \left(\frac{\mathrm{d}\bar{M}_1}{\mathrm{d}x} + \frac{\mathrm{i}\omega}{\bar{c}_1}\right) l\mathrm{e}^{\mathrm{i}\omega(t-T_0)}H(t-T_0). \tag{2.2}$$

The first term in the brackets on the right-hand side is due to shock displacement and the second is due to shock velocity.

Applying the normal shock equations gives, for example, the velocity just downstream of the shock in the moving frame to be

$$u_{2,sh}(h_s,t) \approx -\frac{\bar{c}_1}{(\gamma+1)\bar{M}_1}((\gamma-1)\bar{M}_1^2+2) - \frac{1}{(\gamma+1)\bar{M}_1^2}\left(-2\bar{c}_1\frac{\mathrm{d}\bar{M}_1}{\mathrm{d}x} + \mathrm{i}\omega((\gamma-1)\bar{M}_1^2-2)\right)l\mathrm{e}^{\mathrm{i}\omega(t-T_0)}H(t-T_0)$$

which is equivalent to

$$u_2(h_s,t) \approx -\frac{\bar{c}_1}{(\gamma+1)\bar{M}_1}((\gamma-1)\bar{M}_1^2+2) + \frac{2}{(\gamma+1)\bar{M}_1^2}\left(\bar{c}_1\frac{\mathrm{d}\bar{M}_1}{\mathrm{d}x} + \mathrm{i}\omega(\bar{M}_1^2+1)\right)l\mathrm{e}^{\mathrm{i}\omega(t-T_0)}H(t-T_0) \tag{2.3}$$

in the fixed frame; γ is the ratio of specific heat capacities which is about 1.4 for air. The velocity at the mean shock position, $\bar{h}_s$, can be determined by expanding

$$\begin{aligned} u_2(h_s,t) &\approx u_2(\bar{h}_s,t) + \frac{\partial u_2}{\partial x}(\bar{h}_s,t)l\mathrm{e}^{\mathrm{i}\omega(t-T_0)}H(t-T_0) \\ &\approx \bar{u}_2(\bar{h}_s) + u_2'(\bar{h}_s,t) - \alpha l\mathrm{e}^{\mathrm{i}\omega(t-T_0)}H(t-T_0), \end{aligned}$$

after decomposing $u_2(x,t)$ into its mean value $\bar{u}_2(x)$ and a linear velocity perturbation $u_2'(x,t)$. The last term on the right-hand side is a correction of order $\bar{u}_2$ due to the variation of mean flow with position. Substituting for $u_2(h_s,t)$ in (2.3) and subtracting the mean values, we obtain the velocity perturbation at the mean shock position:

$$u_2'(\bar{h}_s,t) \approx \left(\frac{2}{(\gamma+1)\bar{M}_1^2}\left(\bar{c}_1\frac{\mathrm{d}\bar{M}_1}{\mathrm{d}x} + \mathrm{i}\omega(\bar{M}_1^2+1)\right) + \alpha\right) l\mathrm{e}^{\mathrm{i}\omega(t-T_0)}H(t-T_0). \tag{2.4}$$

The entropy and stagnation enthalpy fluctuations at the mean shock position just downstream of the shock can be related to the shock displacement l and the known function $M_1(x)$ in a similar way. The details are given in Appendix A. The fluctuations of velocity (2.4), entropy (A 3), and total enthalpy (A 4) at the mean shock position provide three boundary conditions for the stagnation flow region. In the next subsection, we have three partial differential equations: entropy equation (2.5), Howe's second-order wave equation (2.7), and Crocco's equation (2.8). These equations, together with the fourth boundary condition of a rigid plate at $x = 0$, form a complete system for the eigenfrequency ω of the linear stability theory.

2.3. *The entropy fluctuation and the solution of the wave equation in the stagnation flow region*

In this subsection, we drop the subscript 2 since only the stagnation flow region is involved. The entropy fluctuations generated by the oscillating shock are convected through the stagnation flow region. After linearizing and neglecting viscosity and heat conductivity, the governing equation for the entropy fluctuation in this region is

$$\frac{\partial S'}{\partial t} + \bar{u}\frac{\partial S'}{\partial x} + \bar{v}\frac{\partial S'}{\partial r} = 0. \tag{2.5}$$

Solving (2.5) with the boundary condition (A 3) and the mean flow in (2.1), we find

$$S'(x,t) = \mathscr{S}\left(\frac{x}{\bar{h}_s}\right)^{i\omega/\alpha} l e^{i\omega(t-T_0)} H\left(t - T_0 + \frac{1}{\alpha}\ln\frac{x}{\bar{h}_s}\right), \tag{2.6}$$

where $\mathscr{S}$ is defined in Appendix A. Note that the Heaviside function ensures that entropy fluctuations do not reach the wall ($x = 0$).

Howe (1975) gives the exact equation for the stagnation enthalpy B, in an inviscid irrotational flow of an ideal non-conducting gas:

$$\left(\frac{\mathrm{D}}{\mathrm{D}t}\left(\frac{1}{c^2}\frac{\mathrm{D}}{\mathrm{D}t}\right) + \frac{1}{c^2}\frac{\mathrm{D}\boldsymbol{u}}{\mathrm{D}t}\cdot\frac{\partial}{\partial \boldsymbol{x}} - \nabla^2\right) B = -\mathrm{div}(T\ \mathrm{grad}\ S) + \frac{1}{c^2}\frac{\mathrm{D}\boldsymbol{u}}{\mathrm{D}t}\cdot(T\ \mathrm{grad}\ S).$$

In this equation, $\mathrm{D}/\mathrm{D}t$ is the material derivative involving the total fluid velocity $\boldsymbol{u}$ and c is the local speed of sound. After linearizing and ignoring the $O(\bar{M}_2^2)$ terms, we obtain a simple wave equation which applies throughout the stagnation flow region:

$$\left(\frac{1}{\bar{c}^2}\left(\frac{\partial}{\partial t} + \bar{\boldsymbol{u}}\cdot\nabla\right)^2 - \nabla^2\right) B' = -\bar{T}\frac{\partial^2}{\partial x^2}S', \tag{2.7}$$

where S' is given in (2.6). The linear operator on the left-hand side of (2.7) describes the propagation of sound waves in the mean flow field $\bar{\boldsymbol{u}}$. The right-hand side identifies entropy fluctuations in the stagnation region as an additional sound source. Just the homogeneous equation form of (2.7) is considered in Mørch's theory.

The boundary condition on the plate at $x = 0$ follows from Crocco's equation for an irrotational flow:

$$\nabla B = -\frac{\partial \boldsymbol{u}}{\partial t} + T\nabla S,$$

which after linearizing simplifies to

$$\frac{\partial B'}{\partial x} = -\frac{\partial u'}{\partial t} + \bar{T}\frac{\partial S'}{\partial x}. \tag{2.8}$$

Imposing the hard-wall boundary conditions $u = 0$ on $x = 0$ and noting that (2.6) states $\partial S/\partial x = 0$ on $x = 0$, we obtain the boundary condition on the wall:

$$\left.\frac{\partial B'}{\partial x}\right|_{x=0} = 0. \tag{2.9}$$

The wave equation (2.7) is greatly simplified by employing a Taylor transformation (Taylor 1978), which defines new variables

$$\boldsymbol{X} = \boldsymbol{x}, \qquad \mathscr{T} = t + \frac{\bar{\phi}}{\bar{c}^2},$$

where $\bar{\phi}$ is the mean flow velocity potential (2.1). Then

$$\frac{\partial}{\partial t}\Big|_x = \frac{\partial}{\partial \mathscr{T}}\Big|_X \quad \text{and} \quad \frac{\partial}{\partial x_i}\Big|_t = \frac{\partial}{\partial X_i}\Big|_{\mathscr{T}} + \frac{1}{\bar{c}^2}\frac{\partial \bar{\phi}}{\partial x_i}\frac{\partial}{\partial \mathscr{T}}\Big|_X.$$

This gives the transformed equation

$$\frac{1}{\bar{c}^2}\frac{\partial^2 B'}{\partial \mathscr{T}^2} - \nabla_X^2 B' = g(\boldsymbol{X}, \mathscr{T}) \tag{2.10}$$

whose accuracy is still correct to $O(\bar{M}_2^2)$, and where ∇_X^2, and $g(\boldsymbol{X}, \mathscr{T})$ are respectively the Laplacian operator and the known source in the new coordinate. The boundary condition is then

$$\frac{\partial B'}{\partial X} = 0 \qquad \text{at} \quad X = 0. \tag{2.11}$$

With the aid of the three-dimensional Green's function, the solution to (2.10) satisfying (2.11) can be easily expressed as

$$B(\boldsymbol{X}, \mathscr{T}) = P(\mathscr{T} - \boldsymbol{X}/\bar{c}) + P(\mathscr{T} + \boldsymbol{X}/\bar{c}) + \frac{\bar{c}}{4\pi}\int_{-\infty}^{\infty}\int_{\mathscr{V}'} g(\boldsymbol{X}', \mathscr{T}') \times \left(\frac{\delta(\bar{c}(\mathscr{T} - \mathscr{T}') - |\boldsymbol{X} - \boldsymbol{X}'|)}{|\boldsymbol{X} - \boldsymbol{X}'|} + \frac{\delta(\bar{c}(\mathscr{T} - \mathscr{T}') - |\boldsymbol{X} - \boldsymbol{X}'^*|)}{|\boldsymbol{X} - \boldsymbol{X}'^*|}\right) \mathrm{d}\mathscr{V}'\mathrm{d}\mathscr{T}' \tag{2.12}$$

where $\mathscr{V}'$ is the mean volume of the stagnation flow region, and $\boldsymbol{X}'^* = (-X', R', \Theta')$ is the image point of $\boldsymbol{X}' = (X', R', \Theta')$.

The first two terms on the right-hand side of (2.12) are upstream and downstream travelling free sound waves. The integral represents the acoustic waves generated by the inhomogeneous entropy source. Mørch's analysis includes the free sound waves, but neglects the acoustic waves due to the entropy inhomogeneity.

We are particularly interested in the wave field near the central axis. For $R = 0\,(= r)$ in (2.12), the integral over Θ' can be readily evaluated. Then reverting to the original coordinate, we obtain

$$B'(x, 0, t) = P\left(t - \frac{x}{\bar{c}}\left(1 + \frac{\alpha x}{2\bar{c}}\right)\right) + P\left(t + \frac{x}{\bar{c}}\left(1 - \frac{\alpha x}{2\bar{c}}\right)\right) + Q(x, t) + Q(-x, t), \tag{2.13}$$

where

$$Q(x, t) = -\frac{\bar{T}\bar{c}}{2}\int_{-\infty}^{\infty}\mathrm{d}t'\int_0^{\bar{h}_s}\mathrm{d}x'\frac{\partial^2 S'}{\partial x'^2} \times \int_0^{\infty} r'\mathrm{d}r'\frac{\delta(\bar{c}(t - t') - (\alpha/2\bar{c})(x^2 - x'^2) - (\alpha/4\bar{c})r'^2 - ((x - x')^2 + r'^2)^{1/2})}{((x - x')^2 + r'^2)^{1/2}}.$$

Normal modes are described by letting $t - T_0 \to \infty$, i.e. by examining the system response a sufficiently long time after the initial excitation. Then the integrals in (2.13) can be calculated. The tedious routine procedures are relegated to Appendix B,

and the final result is

$$B'(x,t) = \tilde{P}\left(t - \frac{x}{\bar{c}}\left(1 + \frac{\alpha x}{2\bar{c}}\right)\right) + \tilde{P}\left(t + \frac{x}{\bar{c}}\left(1 - \frac{\alpha x}{2\bar{c}}\right)\right) + \bar{T}S'(x,t)$$
$$- \frac{\bar{T}x}{4}\frac{\mathrm{i}\omega}{\alpha\bar{h}_s}\mathscr{C}(\omega)\Big(S'(\bar{h}_s, t + x/\bar{c} - \eta(x)) - S'(\bar{h}_s, t - x/\bar{c} - \eta(x))\Big)$$
$$- \frac{\bar{T}x}{4}\frac{\alpha}{\bar{c}}\Big(S'(\bar{h}_s, t + x/\bar{c} - \eta(x)) - S'(\bar{h}_s, t - x/\bar{c} - \eta(x))\Big)$$
$$- \frac{\bar{T}\alpha}{4\bar{c}}\int_{x_f}^{\bar{h}_s} \mathrm{d}x' \left(S'\left(x', t - \frac{\alpha}{2\bar{c}^2}(x^2 - x'^2) - \frac{1}{\bar{c}}|x - x'|\right)\right.$$
$$\left. + S'\left(x', t - \frac{\alpha}{2\bar{c}^2}(x^2 - x'^2) - \frac{1}{\bar{c}}|x + x'|\right)\right), \tag{2.14}$$

where $\eta(x) = \bar{h}_s/\bar{c} + \frac{1}{2}\alpha(x^2 - \bar{h}_s^2)/\bar{c}^2$ and $\mathscr{C}(\omega)$ is $\mathrm{e}^{\mathrm{i}\omega/\alpha}(\mathrm{i}\omega/\alpha)^{1/2}\Gamma(-1/2, \mathrm{i}\omega/\alpha)$. $\Gamma(a,b)$ is the incomplete Gamma function and the branch cut is chosen along the positive imaginary axis of ω. Non-oscillatory, monotonically decaying transient terms have been discarded and x_f defined in Appendix B is exponentially small since $t - T_0 \to \infty$.

The function $\tilde{P}$ describes sound waves travelling in the stagnation region and being reflected in the plane wall. It will be determined in §2.4 by the boundary conditions at the shock position. The third term on the right-hand side of (2.14) is the contribution to $B'(x,t)$ from the local entropy fluctuations. The fourth term results from the time integral of entropy gradient at the mean shock position $\bar{h}_s$. This term is of great importance for low-frequency modes and decays exponentially as $|\omega|$ increases. The fifth term is of $O(\bar{M}_2)$ from the entropy fluctuation at $\bar{h}_s$. Finally, the last term, which is again of $O(\bar{M}_2)$, is the integral of the entropy contribution in the stagnation flow region at the retarded time.

2.4. *The derivation of the characteristic equation*

The total enthalpy fluctuations in the stagnation flow region are described by (2.14) and the unsteady velocity then follows from (2.8). Equations (2.4) and (A 4) provide two boundary conditions for these fluctuations at the mean shock position. After eliminating the function $\tilde{P}$ between these two equations, we will finally obtain an equation for the complex eigenfrequency ω. This is the characteristic equation of linear stability theory and its roots can be readily determined numerically. The details are as follows.

The total enthalpy fluctuation (2.14) at $x = \bar{h}_s$ is

$$B_2'(t) = \tilde{P}\left(t - \frac{\bar{h}_s}{\bar{c}}\left(1 + \frac{\alpha\bar{h}_s}{2\bar{c}}\right)\right) + \tilde{P}\left(t + \frac{\bar{h}_s}{\bar{c}}\left(1 - \frac{\alpha\bar{h}_s}{2\bar{c}}\right)\right) + \bar{T}S_2'(t)$$
$$- \frac{\bar{T}}{4}\frac{\mathrm{i}\omega}{\alpha}\mathscr{C}(\omega)\left(S_2'(t) - S_2'\left(t - \frac{2\bar{h}_s}{\bar{c}}\right)\right)$$
$$- \frac{\bar{T}}{4}\frac{\alpha\bar{h}_s}{\bar{c}}\left(S_2'(t) - S_2'\left(t - \frac{2\bar{h}_s}{\bar{c}}\right)\right) - \frac{\bar{T}\alpha\bar{h}_s}{2\bar{c}}\mathscr{D}(\omega)S_2'\left(t - \frac{\bar{h}_s}{\bar{c}}\right) \tag{2.15}$$

where

$$\mathscr{D}(\omega) = \frac{1}{2}\sum_{j=1}^{\infty} \frac{\mathrm{e}^{\mathrm{i}\omega\bar{h}_s/\bar{c}}(-\mathrm{i}\omega\bar{h}_s/\bar{c})^{(j-1)} + \mathrm{e}^{-\mathrm{i}\omega\bar{h}_s/\bar{c}}(\mathrm{i}\omega\bar{h}_s/\bar{c})^{(j-1)}}{(\mathrm{i}\omega/\alpha + 1)(\mathrm{i}\omega/\alpha + 2)\ldots(\mathrm{i}\omega/\alpha + j)}.$$

The evaluation of the integral over the stagnation region to obtain $\mathscr{D}(\omega)$ is described

in Appendix C. We abbreviate $S_2'(\bar{h}_s,t)$, $B_2'(\bar{h}_s,t)$, $u_2'(\bar{h}_s,t)$ to $S_2'(t)$, $B_2'(t)$, and $u_2'(t)$, respectively, and these are all given in terms of the shock displacement l by (2.4), (A 3), and (A 4); $\bar{c}$ is the sound speed in the stagnation flow region.

Substituting (2.14) into (2.8), we can easily obtain the velocity fluctuation at the mean shock position:

$$\begin{aligned} u_2'(t) = {} & \frac{1}{\bar{c}}\left(1+\frac{\alpha\bar{h}_s}{\bar{c}}\right)\tilde{P}\left(t-\frac{\bar{h}_s}{\bar{c}}\left(1+\frac{\alpha\bar{h}_s}{2\bar{c}}\right)\right) - \frac{1}{\bar{c}}\left(1-\frac{\alpha\bar{h}_s}{\bar{c}}\right)\tilde{P}\left(t+\frac{\bar{h}_s}{\bar{c}}\left(1-\frac{\alpha\bar{h}_s}{2\bar{c}}\right)\right) \\ & + \frac{\bar{T}}{4}\mathscr{C}(\omega)\left(\frac{1}{\alpha\bar{h}_s}\left(S_2'(t)-S_2'\left(t-\frac{2\bar{h}_s}{\bar{c}}\right)\right)\right. \\ & \qquad \left. + \frac{\mathrm{i}\omega}{\alpha\bar{c}}\left(\left(1-\frac{\alpha\bar{h}_s}{\bar{c}}\right)S_2'(t)+\left(1+\frac{\alpha\bar{h}_s}{\bar{c}}\right)S_2'\left(t-\frac{2\bar{h}_s}{\bar{c}}\right)\right)\right) \\ & + \frac{\bar{T}\alpha}{4\mathrm{i}\omega\bar{c}}\left(S_2'(t)-S_2'\left(t-\frac{2\bar{h}_s}{\bar{c}}\right)\right) + \frac{\bar{T}\alpha\bar{h}_s}{4\bar{c}^2}\left(S_2'(t)+S_2'\left(t-\frac{2\bar{h}_s}{\bar{c}}\right)\right) \\ & - \frac{\bar{T}\alpha\bar{h}_s}{2\bar{c}^2}\mathscr{D}(\omega)S_2'\left(t-\frac{\bar{h}_s}{\bar{c}}\right). \end{aligned} \tag{2.16}$$

Equations (2.15) and (2.16) may be rearranged into equations for the travelling wave $\tilde{P}$. They are

$$\frac{2}{\bar{c}}\tilde{P}\left(t+\frac{\bar{h}_s}{\bar{c}}\left(1-\frac{\alpha\bar{h}_s}{2\bar{c}}\right)\right) = \frac{1}{\bar{c}}\left(1+\frac{\alpha\bar{h}_s}{\bar{c}}\right)B_2'(t) - u_2'(t) + \mathscr{Q}'(t), \tag{2.17}$$

and

$$\frac{2}{\bar{c}}\tilde{P}\left(t-\frac{\bar{h}_s}{\bar{c}}\left(1+\frac{\alpha\bar{h}_s}{2\bar{c}}\right)\right) = \frac{1}{\bar{c}}\left(1-\frac{\alpha\bar{h}_s}{\bar{c}}\right)B_2'(t) + u_2'(t) + \mathscr{R}'(t), \tag{2.18}$$

where the terms $\mathscr{Q}'(t)$ and $\mathscr{R}'(t)$ describe the entropy terms, with

$$\begin{aligned} \mathscr{Q}'(t) = {} & -\frac{1}{\bar{c}}\left(1+\frac{\alpha\bar{h}_s}{\bar{c}}\right)\bar{T}S_2'(t) \\ & + \frac{\bar{T}}{4}\mathscr{C}(\omega)\left(\frac{1}{\alpha\bar{h}_s}\left(S_2'(t)-S_2'\left(t-\frac{2\bar{h}_s}{\bar{c}}\right)\right)+\frac{2\mathrm{i}\omega}{\alpha\bar{c}}S_2'(t)\right) \\ & + \frac{\bar{T}\alpha}{4\bar{c}}\left(\frac{\bar{h}_s}{\bar{c}}+\frac{1}{\mathrm{i}\omega}\right)\left(S_2'(t)-S_2'\left(t-\frac{2\bar{h}_s}{\bar{c}}\right)\right) + \frac{\bar{T}\alpha\bar{h}_s}{4\bar{c}^2}\left(S_2'(t)+S_2'\left(t-\frac{2\bar{h}_s}{\bar{c}}\right)\right), \end{aligned}$$

and

$$\begin{aligned} \mathscr{R}'(t) = {} & -\frac{1}{\bar{c}}\left(1-\frac{\alpha\bar{h}_s}{\bar{c}}\right)\bar{T}S_2'(t) \\ & - \frac{\bar{T}}{4}\mathscr{C}(\omega)\left(\frac{1}{\alpha\bar{h}_s}\left(S_2'(t)-S_2'\left(t-\frac{2\bar{h}_s}{\bar{c}}\right)\right)+\frac{2\mathrm{i}\omega}{\alpha\bar{c}}S_2'\left(t-\frac{2\bar{h}_s}{\bar{c}}\right)\right) \\ & + \frac{\bar{T}\alpha}{4\bar{c}}\left(\frac{\bar{h}_s}{\bar{c}}-\frac{1}{\mathrm{i}\omega}\right)\left(S_2'(t)-S_2'\left(t-\frac{2\bar{h}_s}{\bar{c}}\right)\right) - \frac{\bar{T}\alpha\bar{h}_s}{4\bar{c}^2}\left(S_2'(t)+S_2'\left(t-\frac{2\bar{h}_s}{\bar{c}}\right)\right) \\ & + \frac{\bar{T}\alpha\bar{h}_s}{\bar{c}^2}\mathscr{D}(\omega)S_2'\left(t-\frac{\bar{h}_s}{\bar{c}}\right). \end{aligned}$$

Equation (2.17) relates $\tilde{P}$ to flow parameters at the shock at an earlier time, and

so describes the effect of waves reflected from the rigid surface. On the other hand, through (2.18), $\tilde{P}$ is expressed in terms of later flow perturbations. Equations (2.17) and (2.18) can be recast to give $\tilde{P}$ at a common reference time τ, by substituting $t = \tau - \bar{h}_s/\bar{c}$, $t = \tau + \bar{h}_s/\bar{c}$ into (2.17) and (2.18), respectively. Then

$$\frac{2}{\bar{c}} e^{-i\omega\alpha\bar{h}_s^2/2\bar{c}^2} \tilde{P}(\tau) = \frac{1}{\bar{c}}\left(1 + \frac{\alpha\bar{h}_s}{\bar{c}}\right) B_2'\left(\tau - \frac{\bar{h}_s}{\bar{c}}\right) - u_2'\left(\tau - \frac{\bar{h}_s}{\bar{c}}\right) + \mathscr{Q}'\left(\tau - \frac{\bar{h}_s}{\bar{c}}\right) \quad (2.19)$$

and

$$\frac{2}{\bar{c}} e^{-i\omega\alpha\bar{h}_s^2/2\bar{c}^2} \tilde{P}(\tau) = \frac{1}{\bar{c}}\left(1 - \frac{\alpha\bar{h}_s}{\bar{c}}\right) B_2'\left(\tau + \frac{\bar{h}_s}{\bar{c}}\right) + u_2'\left(\tau + \frac{\bar{h}_s}{\bar{c}}\right) + \mathscr{R}'\left(\tau + \frac{\bar{h}_s}{\bar{c}}\right). \quad (2.20)$$

All the terms on the right-hand sides of (2.19) and (2.20) are proportional to the shock displacement l (see (2.4), (A 3), (A 4)).

By equating (2.19) and (2.20), we get $\mathscr{F}(\omega)l = 0$ where

$$\mathscr{F}(\omega) = \frac{1}{l}\{\textit{right-hand side of (2.19)} - \textit{right-hand side of (2.20)}\}.$$

This only allows non-zero oscillation amplitude l at discrete frequencies ω which are roots of the characteristic equation

$$\mathscr{F}(\omega) = 0. \quad (2.21)$$

The roots and stability margins of the characteristic equation are investigated in the next two subsections.

2.5. *Roots of the characteristic equation*

It is convenient to non-dimensionalize the physical quantities on the diameter of the nozzle lip and the stagnation sound speed. From now on, the symbols ω, $\bar{h}_s$, x_{res}, etc. denote the non-dimensional quantities. The characteristic equation (2.21) involves the Mach number and its slope just upstream of the mean shock position. For a particular mean shock position $\bar{h}_s$ and the nozzle-to-plate distance x_{res}, we can use the free jet axial Mach number function (shown in figure 2) at a distance $x_{res} - \bar{h}_s$ from the nozzle to determine the Mach number and its slope just upstream of the standoff shock. Once the mean flow is known, the eigenfrequencies of linear oscillations can be determined by searching for the roots of (2.21) in the complex frequency domain. For example, for the case $x_{res} = 1.30$, $\bar{h}_s = 0.56$, and $p_0/p_a = 3.72$, for which $\bar{M}_1 = 2.13$, and $d\bar{M}_1/dx = -1.69$, figure 3 shows that there are isolated roots scattered in the search region. These modes are numbered according to the magnitude of their real frequencies. In this case, all of the modes obtained are stable and can be classified into two families by the different ranges of their damping rate. The family with smaller damping rates (the odd modes) are likely to be observed experimentally. In each family, the modes with higher frequencies tend to be more stable. Figure 4 shows the case for which $x_{res} = 1.30$, $\bar{h}_s = 0.31$, $p_0/p_a = 3.72$, leading to $\bar{M}_1 = 2.60$, and $d\bar{M}_1/dx = -0.90$. In this case, an unstable mode is found, which grows exponentially according to linear theory.

In this section we have arbitrarily chosen two values of $\bar{h}_s$ for the examples in figures 3 and 4 to illustrate that the characteristic equation has both stable and unstable roots (although the first case is close to the shock position observed for the jet impinging on a plane surface and the latter case $\bar{h}_s = 0.31$ has been observed when the jet impinges on a small plate of diameter $D/d = 0.3$, Mørch 1963). In §2.6, we map out the stability margins as a function of $\bar{h}_s$ and x_{res}, and in §4, we combine

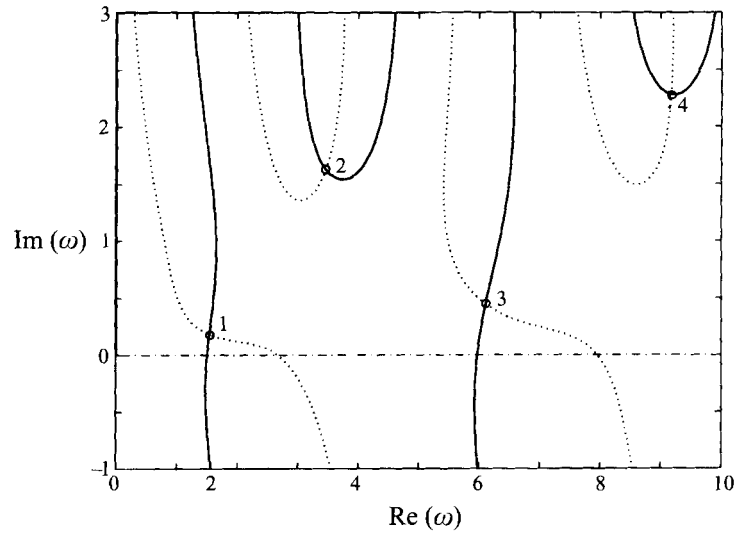

FIGURE 3. Roots of the characteristic equation for the case $x_{res} = 1.3$, $\bar{h}_s = 0.56$, $p_0/p_a = 3.72$, $\bar{M}_1 = 2.13$, $d\bar{M}_1/dx = -1.69$. —, Contour lines of $\mathrm{Re}(\mathscr{F}) = 0$; ···, contour lines of $\mathrm{Im}(\mathscr{F}) = 0$; ○, roots of $\mathscr{F} = 0$.

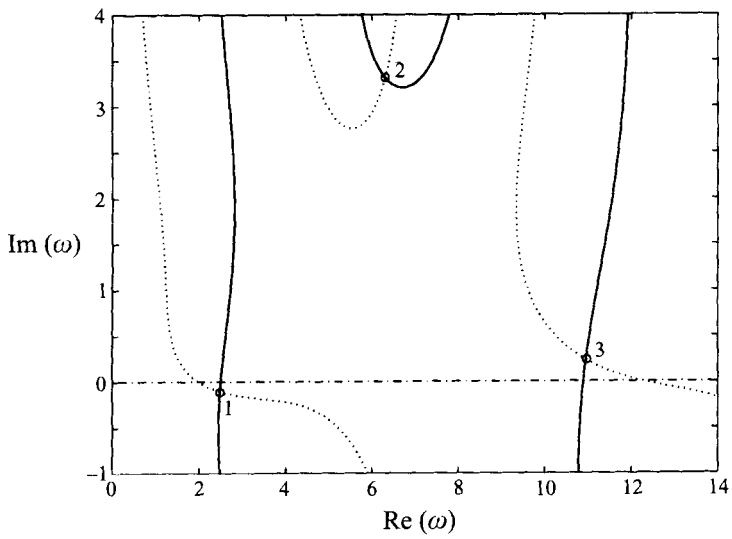

FIGURE 4. Roots of the characteristic equation for the case $x_{res} = 1.30$, $\bar{h}_s = 0.31$, $p_0/p_a = 3.72$, $\bar{M}_1 = 2.60$, $d\bar{M}_1/dx = -0.90$. —, Contour lines of $\mathrm{Re}(\mathscr{F}) = 0$; ···, contour lines of $\mathrm{Im}(\mathscr{F}) = 0$; ○, roots of $\mathscr{F} = 0$.

our stability map with particular values of $\bar{h}_s$ that occur in a range of practical configurations to compare with experimental results.

2.6. *Stability margin diagram*

In this subsection, we are only concerned with the least-stable mode (mode 1). As we saw in §2.5, the complex eigenfrequency ω can be determined for specified values of $\bar{h}_s$ and x_{res}. By varying $\bar{h}_s$ and x_{res} over a specific range, we can therefore obtain the contours of the imaginary part of ω, as shown in figure 5. In this figure, x_{res}

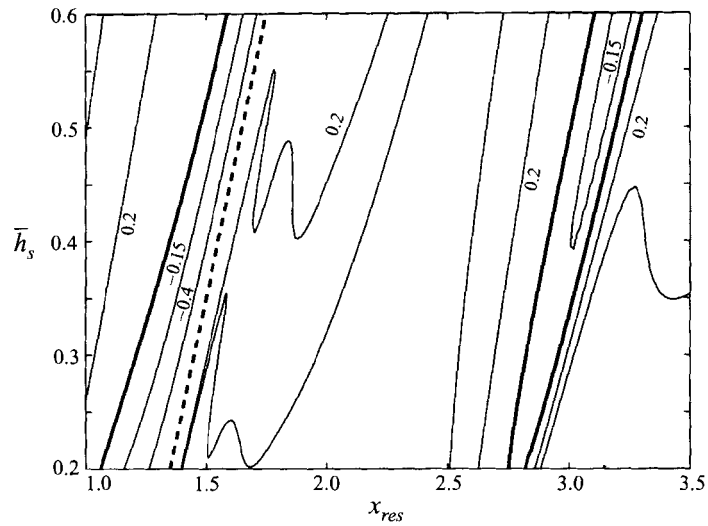

FIGURE 5. Stability margin diagram for the case $p_0/p_a = 3.72$. —, Contour lines of $\mathrm{Im}(\omega)$ of the least-stable mode; —, neutral stability curves; – – –, the free jet shock and a boundary between unstable and stable flow.

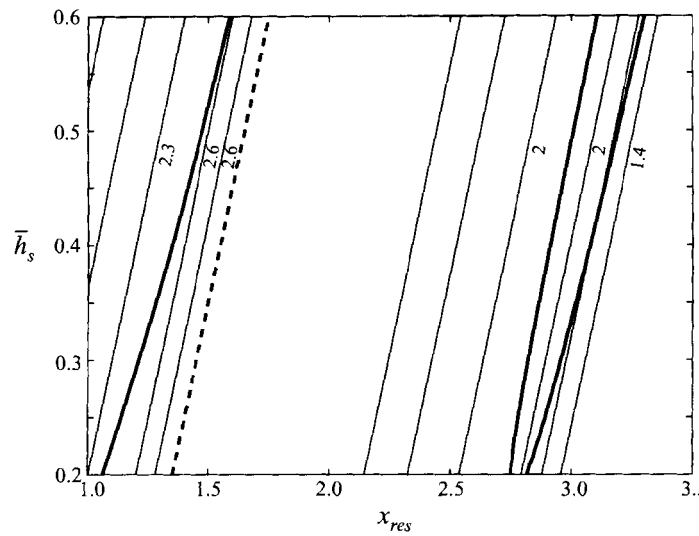

FIGURE 6. Mach number contour lines just upstream of the standoff shock at the given $\bar{h}_s$ and x_{res} for the case $p_0/p_a = 3.72$. —, Mach number contour lines; —, neutral stability curves; – – –, the free jet shock and a boundary between unstable and stable flow.

varies roughly over the first two shock cells. Two unstable strips are found, where the damping rate is negative. For values of $\bar{h}_s$ and x_{res} in these strips, linear theory predicts that the unstable mode grows exponentially, but in practice it would be limited by nonlinear mechanisms. It may result in the finite-amplitude bistable shock motion observed by Powell (1988).

The Mach number in front of the shock is shown as a function of $\bar{h}_s$ and x_{res} in figure 6. The neutral stability curves have been superimposed in this figure. By comparing the stability margins with the Mach contour lines, we find that the standoff

shock is unstable when it lies in the downstream portion of each free jet shock cell. This is in excellent agreement with Powell's (1988) observation of a repetitive pattern of unstable regions. The maximum growth rate occurs when the standoff shock lies just upstream of where a conical shock would form in the free jet. Positions at which the standoff shock is unstable are illustrated as a function of upstream Mach number in figure 2.

Figures 5 and 6 summarize how the standoff shock position influences its stability. However, to predict the eigenfrequency for a particular plate and nozzle-to-plate distance x_{res}, we need to know the mean shock position $\bar{h}_s$. This could be determined experimentally or from approximate integral methods (Gummer & Hunt 1971; Shapiro 1954). Instead, we use results from a numerical simulation, which is described in the next section.

3. Numerical simulation and results

The numerical simulation uses Denton's second-order-explicit finite volume code for unsteady axisymmetric inviscid flow (Denton 1993). We use 110 and 85 grid points in the radial and axial directions respectively. This mesh size varies slightly in different cases. The sizes of mesh elements increase gradually with their distance from the jet boundary. The finest spatial resolution is 0.010 by 0.023 and the time step has to be less than 0.010 to satisfy the Courant–Friedrichs–Lewy condition, which states that the maximum time step has to be less than the minimum time for sound to travel through the smallest calculation elements. Experimental observations of the standoff shock oscillation suggest that the non-dimensionalized frequency of disturbances is roughly 2. This unsteadiness can be sufficiently resolved by the mesh we use.

The boundary conditions applied are sonic conditions, with known stagnation pressure and temperature at the nozzle exit, together with rigid wall boundary conditions over the rest of the nozzle exit plane and on the plate. Conditions of constant static pressure and no incoming mass flux are applied at calculation boundaries far from the jet. We first use this numerical scheme to obtain the details of the mean flow required in the linear stability analysis described in §2. Secondly, we investigate the finite-amplitude oscillations that develop in this unsteady simulation. Checks were made to ensure that the frequency of oscillation is independent of the size of the computational domain. The outer radius R_∞ of the computational domain was increased from 4.0 to 7.0, with negligible effect on the frequency of oscillation. Moreover, we find that the frequency of oscillation agrees well with that predicted from linear theory. This gives us confidence in the numerical results and we use the simulation to investigate the effect of replacing the infinite plate by different downstream reflectors.

When this jet impinges on an infinite plate a strong standoff shock is formed. A typical instantaneous flow field near the plate at $x_{res} = 1.3$ and $p_0/p_a = 3.72$ is illustrated in figure 7. The mean standoff shock position is $\bar{h}_s = 0.55$. By rerunning the code for different values of x_{res}, we can obtain the mean shock wave positions $\bar{h}_s$ as functions of x_{res} as shown in figure 8. These functions will be used with the linear theory of §2 to find eigenfrequencies of shock oscillation. Mørch's experimental data are shown for comparison in figure 8. We find a reasonable agreement and a similar trend of the function in the overlap region. Having established that the numerical calculation agrees well with experimental data, we can use the detailed information it gives to check the assumptions made about the mean flow in the development of the linear stability theory in §2. Note that velocity vectors in figure 7 show that the

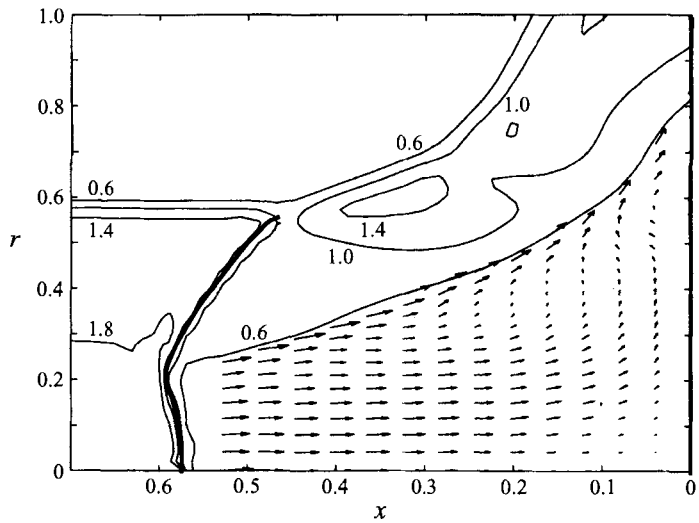

FIGURE 7. Mach number contours and velocity field of the stagnation flow region at $t = 178$, $x_{res} = 1.3$ and $p_0/p_a = 3.72$. —, Mach number contour line; →, velocity vector. The computational domain extends to $r = 5.0$

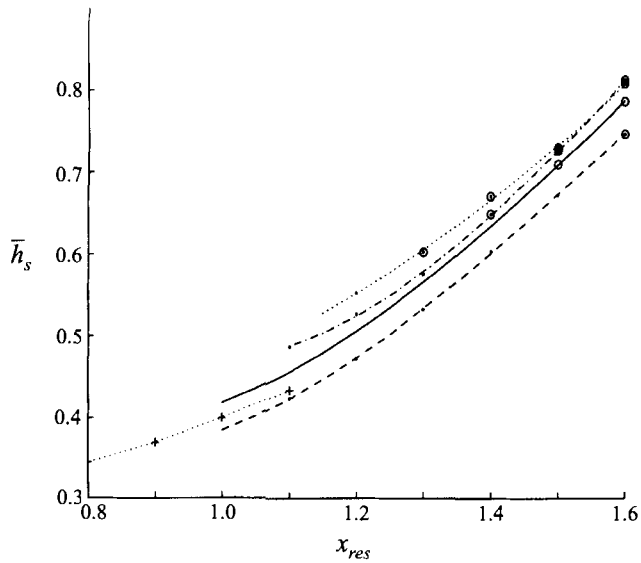

FIGURE 8. Mean shock position functions for $p_0/p_a = 3.72$: —, infinite plate; — — —, $D/d = 1.0$; —·—, $D/d = 2.0$; · · ·, $D/d = 3.0$. +···+, Mørch's experimental data for $D/d = 1.0$ and $p_0/p_a = 3.83$. ○, Recirculating bubbles appear near to the plate.

stagnation flow has no recirculation bubble. The mean velocity in the stagnation flow region (figure 9) also shows a good agreement with the incompressible stagnation flow approximation. We also find a supersonic discharge flow region which extends from the edge of the standoff shock and is known as a supersonic near-wall jet (Carling & Hunt 1974).

Figure 10 shows the pressure fluctuations calculated in the numerical simulation for $p_0/p_a = 3.72$ and $x_{res} = 1.3$. Results are shown for three positions: on the jet

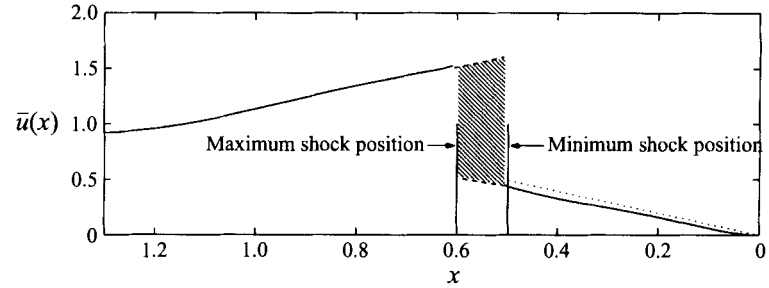

FIGURE 9. Mean velocity on the central axis for $x_{res} = 1.3$. $\cdots$. The incompressible stagnation flow approximation.

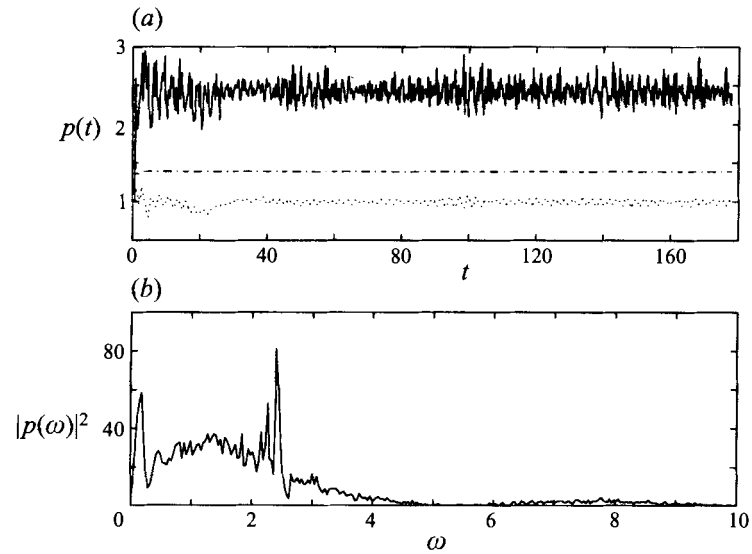

FIGURE 10. (*a*) Pressure versus time: —, at the origin; — · —, at $x = 0.96$ and $r = 0$; $\cdots$, at $x = 0.96$ and $r = 1.36$. (*b*) Power spectrum of pressure fluctuation at the origin.

centreline on the plate, halfway between the standoff shock and the nozzle, and at a point outside the jet. These pressures are normalized by ambient pressure. The fluctuations at the latter two points are much smaller than those at the origin showing that the major oscillations occur near the jet centreline in the stagnation flow region. The frequency of oscillation can be determined from a Fourier transform of these time histories and the spectrum of the pressure fluctuation on the plate is shown in figure 10. There is a strong peak near a non-dimensional frequency of 2. The mode involves variation in axial position of the shock as in the linear theory. By varying x_{res}, we obtain the range of frequencies of shock oscillation shown in figure 11.

In §4, we will compare these frequencies with experimental results. The experiments are for jets impinging on plates of small or moderate diameter D. We have modified the numerical scheme to consider a jet incident on the end plate of a rigid cylinder of diameter D as sketched as in figure 1. We can again obtain the mean shock position $\bar{h}_s$ as a function of nozzle-to-plate distance x_{res} and the plate size D as in figure 8. We have also marked the cases where the calculated stagnation flow has a recirculation bubble. Similar recirculation bubbles have been observed when a uniform jet impinges on a flat surface (Kalghatgi & Hunt 1976). According to

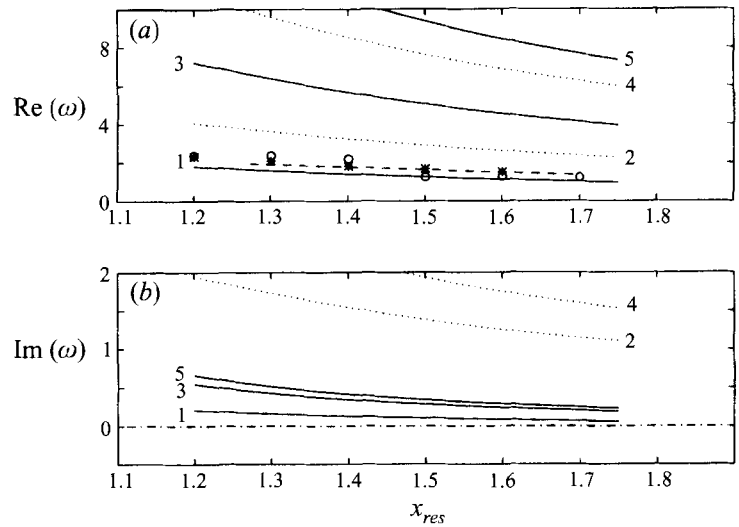

FIGURE 11. Oscillation frequency and comparison with experimental data at $p_0/p_a = 3.72$. (*a*) Real part of the complex frequency versus x_{res}; (*b*) damping rate versus x_{res}. —, ···, Theoretical value; – – –, Powell's experimental data; ○, numerical simulated modes for infinite plate; *, numerical simulated modes for $D/d = 1.0$.

Kalghatgi & Hunt's experimental data and their criterion, we note that there, as in the numerical results, the recirculation bubble seems to occur when the shock-to-plate distance exceeds a critical value. Mørch (1973) uses a two-dimensional composite jet model to determine the margin of appearance of the stagnation bubble and terms it a 'blocking phenomenon'. For our case, the bubbles appear roughly when the mean shock position is further than 0.6 from the plate. The oscillation frequencies for the case $D = 1.0$ versus x_{res} are also shown in figure 11. It is clear that plate size does not have a major effect on the frequency of shock oscillation.

4. Comparison with experimental data

In this section, we present results from the theoretical linear stability analysis, and their comparison with the numerical simulation and with experimental data of Powell (1988) and Mørch (1964). We need to justify applying a theory for a jet impinging on an infinite plane surface to experiments with plates of modest diameters less than 4, particularly as the experimenters find jets incident on large plates to be more susceptible to oscillations associated with vortex shedding from the nozzle than to shock-induced oscillations (Powell 1988; Henderson & Powell 1993). However, the experimental results show that when the standoff shock oscillation mode is detectable, its frequency is virtually independent of plate size D (see, for example, Powell 1988, figure 11). The same conclusion can be drawn from the results of the numerical simulation summarized in figure 11. Further evidence that the plate edges do not have a major effect on the frequency is the similarity between Mørch's lowest-frequency mode for plates with sharp corners and Powell's for plates with chamfered edges (see Powell 1988, figure 5). Our theoretical model (and that of Mørch) therefore emphasizes the flow near the jet axis as being crucial in the feedback processes that control the frequency of shock oscillation. The only way

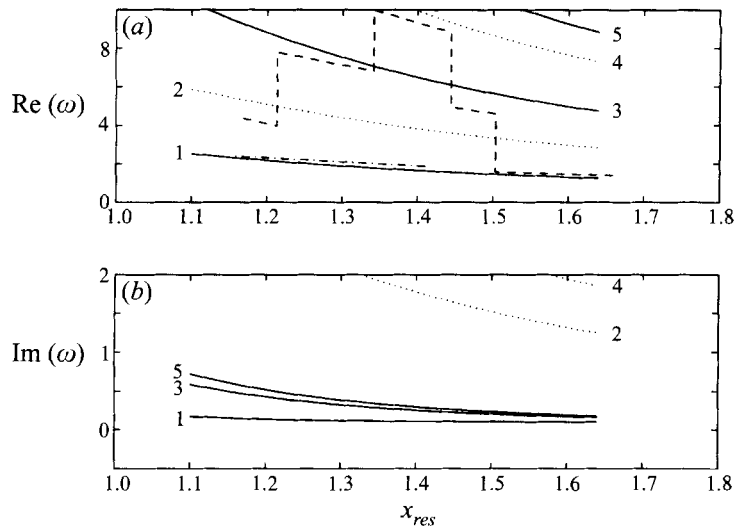

FIGURE 12. Oscillation frequency and comparison with experimental data at $p_0/p_a = 3.83$. (*a*) Real part of the complex frequency versus x_{res}; (*b*) damping rate versus x_{res}. —, ···, Theoretical value; – – –, Mørch's experimental data for $D/d = 0.58$; – · –, Mørch's experimental data for $D/d = 1.0$.

this local flow is influenced by plate size is through the modest changes it induces in $\bar{h}_s$ as shown in figure 8. We therefore believe it entirely appropriate to compare the theoretical predictions for frequency with experimental data for plates of modest size.

First, we investigate the case of Powell (1988) with $p_0/p_a = 3.72$. The mean shock position $\bar{h}_s$ is determined as a function of x_{res} from the numerical simulation (see $D/d = 1.0$ curve in figure 8). The frequencies and damping rates of the lowest three modes versus x_{res} are then obtained by solving the characteristic equation. The results are shown in figure 11. We find that the experimental data and the frequency of oscillation in the numerical simulations are consistent with the lowest eigenfrequency, which is also the least-stable mode. The higher-frequency modes, with higher damping rates, are probably too weak to be detected in Powell's experiment. The second example for comparison is Mørch's data (Mørch 1963, 1964). The pressure ratio is $p_0/p_a = 3.83$ and two different sizes of plate are used. The mean shock position and the Mach number just upstream are both given in his papers (1963, 1964). Using these data directly, we get the theoretical results shown in figure 12. Three of our theoretical branches (modes 1, 3 and 4) agree with measured frequencies. As expected, the branch with the lowest frequency has the largest oscillation amplitude. However, our linear theory is not able to explain why, for the smaller plate case the experimental frequency jumps from one branch to another at certain x_{res}, nor the appearance of the higher mode. This might involve other external feedback mechanisms which are not included in this theory. For example, for the smaller plate, disturbances from the edge of the plate might have an upstream influence and affect the mode selection.

For the two sets of parameters investigated here, all five modes are stable, although the odd modes are only very lightly damped. Self-excited oscillations involving just the standoff shock and the stagnation region cannot be sustained at these flow conditions. However, the response of the shock and stagnation flow to external forcing is highly resonant, with a large response to any excitation near the odd

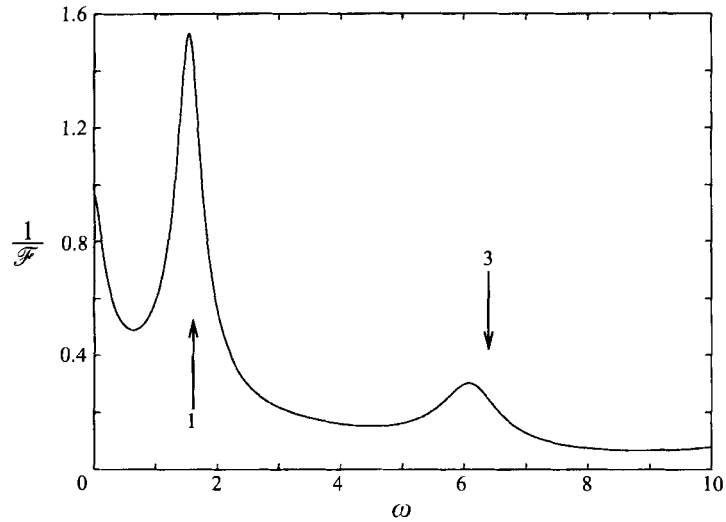

FIGURE 13. The gain function, $1/\mathscr{F}(\omega)$, describing the response to forcing for $x_{res} = 1.3$, $\bar{h}_s = 0.56$, $p_0/p_a = 3.72$, $\bar{M}_1 = 2.13$, $\mathrm{d}\bar{M}_1/\mathrm{d}x = -1.69$. Arrows show the real part of eigenfrequencies of modes 1 and 3.

eigenfrequencies. Without going in the detail of the forcing mechanism, we note that the response of forcing at a real frequency ω is proportional to $1/\mathscr{F}(\omega)$. This function is plotted as a function of ω in figure 13 for $x_{res} = 1.30$, $\bar{h}_s = 0.56$, $p_0/p_a = 3.72$, $\bar{M}_1 = 2.13$, and $\mathrm{d}\bar{M}_1/\mathrm{d}x = -1.69$. It has strong peaks near the real part of the first and third eigenfrequencies, demonstrating how strong the response is to excitation near these frequencies. This mechanism may be relevant to the observation of Henderson & Powell (1993) that, at least for some flow conditions, some form of feedback from the nozzle is required to sustain the shock oscillation, even though the frequency of oscillation is controlled by feedback between the shock and the plate. We expect that this feedback may involve the interaction of acoustic waves with the jet expansion at the nozzle lip, leading to disturbances which propagate downstream in the supersonic jet to sustain the standoff shock oscillation.

5. Conclusion

A linear stability theory has been developed to give physical insight into the self-excited oscillations that can occur when a moderately underexpanded jet impinges on a plate. Oscillations of the standoff shock generate linear pressure and entropy disturbances in the stagnation flow region between the shock and the plate. We find that the entropy fluctuations are a significant acoustic source. As the entropy inhomogeneities are decelerated through the stagnation flow, they generate additional pressure waves which propagate upstream and enhance the shock oscillation. Using the known Mach number variation along the axis of a supersonic jet, which is a function of pressure ratio p_0/p_a, we find a characteristic equation for the eigenfrequencies of the shock oscillation mode. There are two families of isolated roots and the lowest-frequency mode is the least stable. Its frequency varies between about 1 and 2, where we have non-dimensionalized lengths on the diameter of the nozzle exit and velocity on the stagnation sound speed. We determine the threshold at

which this mode becomes unstable as a function of x_{res}, the nozzle-to-plate distance, and $\bar{h}_s$, the standoff distance of the shock from the plate. Instability occurs roughly when the standoff shock is in the downstream section of each shock cell of the underexpanded free jet. This agrees well with experimental observations (Powell 1988).

We have used a numerical simulation to obtain the mean flow parameters needed in the linear stability analysis and to check some of the assumptions made in this simplified theory. For a specified mean shock position, we can solve for the frequencies and damping rates of the oscillation modes by determining the roots of the characteristic equation. We find that the predicted frequencies agree well with the experimental data of Powell and Mørch and with results of the numerical simulation.

The authors wish to express their sincere gratitude to Professor J. D. Denton of the Whittle Laboratory, Cambridge University Engineering Department for providing the program used in the numerical simulation, and for his help and advice with its implementation. This work was carried out while one of the authors (C.-Y. K.) was in receipt of an ORS award from the Committee of Vice-Chancellors and Principals.

Appendix A. Perturbations behind the oscillating normal shock

Using the relative Mach number (2.2) in the normal shock relations, we find that the temperature and entropy downstream of the shock are

$$T_2(h_s,t) \approx \left(1+\frac{2(\gamma-1)}{(\gamma+1)^2}(\gamma\bar{M}_1^2+1)(1-\bar{M}_1^{-2})\right)\bar{T}_1(\bar{h}_s) + \frac{2(\gamma-1)}{(\gamma+1)^2\bar{M}_1^3}\left(((\gamma-1)\bar{M}_1^2+2)\frac{\mathrm{d}\bar{M}_1}{\mathrm{d}x}+\frac{2\mathrm{i}\omega}{\bar{c}_1}(\gamma\bar{M}_1^4+1)\right)\bar{T}_1(\bar{h}_s)l\mathrm{e}^{\mathrm{i}\omega(t-T_0)}H(t-T_0), \tag{A 1}$$

and

$$S_2(h_s,t)-S_1 \approx \left(\frac{1}{\gamma-1}\ln\left(\frac{2\gamma\bar{M}_1^2}{\gamma+1}-\frac{\gamma-1}{\gamma+1}\right)+\frac{\gamma}{\gamma-1}\ln\frac{2+(\gamma-1)\bar{M}_1^2}{(\gamma+1)\bar{M}_1^2}\right)R + 4\gamma R\left(\frac{\mathrm{d}\bar{M}_1}{\mathrm{d}x}+\frac{\mathrm{i}\omega}{\bar{c}_1}\right)\frac{(\bar{M}_1^2-1)^2}{\bar{M}_1(2+(\gamma-1)\bar{M}_1^2)(2\gamma\bar{M}_1^2-\gamma+1)}l\mathrm{e}^{\mathrm{i}\omega(t-T_0)}H(t-T_0), \tag{A 2}$$

where R is the idea gas constant, and we have assumed the flow to be isentropic upstream of the shock.

The physical variable used in the theory is the specific stagnation enthalpy B, which is equal to $c_pT+\frac{1}{2}|\boldsymbol{u}|^2$, where T is the the flow temperature and $\boldsymbol{u}$ is the fluid velocity. After substitution for T_2 and u_2 from (A 1) and (2.3) respectively, the total enthalpy at the shock position is found to be

$$B_2(h_s,t) = c_p\bar{T}_2+\frac{2\mathrm{i}\omega\bar{c}_1}{(\gamma+1)\bar{M}_1}(\bar{M}_1^2-1)l\mathrm{e}^{\mathrm{i}\omega(t-T_0)}H(t-T_0)+O(\bar{M}_2^2),$$

after linearization.

Extrapolating from the instantaneous shock position to $\bar{h}_s$, as described in §2.2, we

can expand the entropy change at the mean shock position as

$$S_2(h_s,t)-S_1=(\bar{S}_2(\bar{h}_s)-S_1)+S_2'(\bar{h}_s,t)+\frac{\partial\bar{S}_2}{\partial x}(\bar{h}_s)l\mathrm{e}^{\mathrm{i}\omega(t-T_0)}H(t-T_0).$$

The last term vanishes since $\bar{S}_2(x)$ is a constant with negligible $O(\bar{M}_2^2)$ spatial variance. The entropy variation across the standoff shock greatly exceeds that in either the upstream supersonic jet or near the axis in the downstream stagnation flow region. The entropy fluctuation at the mean shock position then follows from substitution for $S_2(h_s,t)-S_1$ in (A 2):

$$S_2'(\bar{h}_s,t)=\mathscr{S}l\mathrm{e}^{\mathrm{i}\omega(t-T_0)}H(t-T_0), \tag{A 3}$$

where

$$\mathscr{S}=4\gamma R\left(\frac{\mathrm{d}\bar{M}_1}{\mathrm{d}x}+\frac{\mathrm{i}\omega}{\bar{c}_1}\right)\frac{(\bar{M}_1^2-1)^2}{\bar{M}_1(2+(\gamma-1)\bar{M}_1^2)(2\gamma\bar{M}_1^2-\gamma+1)}.$$

Similarly, we can obtain the total enthalpy fluctuation:

$$B_2'(\bar{h}_s,t)=\frac{2\mathrm{i}\omega\bar{c}_1}{(\gamma+1)\bar{M}_1}(\bar{M}_1^2-1)l\mathrm{e}^{\mathrm{i}\omega(t-T_0)}H(t-T_0). \tag{A 4}$$

Equations (A 3), (A 4) and (2.4) relate perturbations in entropy, stagnation enthalpy, and velocity at the mean shock position to the shock displacement $l\mathrm{e}^{\mathrm{i}\omega(t-T_0)}H(t-T_0)$.

Appendix B. Integration of forced wave components

Carrying out the integral over r', the forced wave component $Q(x,t)$ of (2.13) becomes

$$Q(x,t)=-\frac{\bar{T}\bar{c}}{2}\int_{-\infty}^{\infty}\mathrm{d}t'\int_0^{\bar{h}_s}\mathrm{d}x'\,\frac{\partial^2S'}{\partial x'^2}\times\frac{1}{(1+\alpha(t-t'))^{1/2}}H\left(\bar{c}(t-t')-\frac{\alpha}{2\bar{c}}(x^2-x'^2)-|x-x'|\right) \tag{B 1}$$

where $O(\bar{M}_2^2)$ terms have been omitted. Substituting for the entropy fluctuation from (2.6) and integrating (B 1) with respect to x' by parts gives $Q(x,t)=Q_1(x,t)+Q_2(x,t)$, where

$$Q_1(x,t)=-\frac{\bar{T}\bar{c}}{2}\mathscr{S}l\mathrm{e}^{-\mathrm{i}\omega T_0}\int_{-\infty}^{\infty}\frac{\mathrm{d}t'\,\mathrm{e}^{\mathrm{i}\omega t'}\mathscr{A}}{(1+\alpha(t-t'))^{1/2}}, \tag{B 2}$$

$$Q_2(x,t)=\frac{\bar{T}\bar{c}}{2}\mathscr{S}l\mathrm{e}^{-\mathrm{i}\omega T_0}\int_{-\infty}^{\infty}\frac{\mathrm{d}t'\,\mathrm{e}^{\mathrm{i}\omega t'}\mathscr{B}}{(1+\alpha(t-t'))^{1/2}}. \tag{B 3}$$

with

$$\mathscr{A}=\left(\frac{\mathrm{i}\omega}{\alpha\bar{h}_s}H(t'-T_0)+\frac{1}{\alpha\bar{h}_s}\delta(t'-T_0)\right)H\left(\bar{c}(t-t')-\frac{\alpha}{2\bar{c}}(x^2-\bar{h}_s^2)-(\bar{h}_s-x)\right),$$

$$\mathscr{B}=\int_0^{\bar{h}_s}\left(\frac{\mathrm{i}\omega}{\alpha\bar{h}_s}\left(\frac{x'}{\bar{h}_s}\right)^{(\mathrm{i}\omega/\alpha)-1}H\left(t'-T_0+\frac{1}{\alpha}\ln\frac{x'}{\bar{h}_s}\right)+\frac{1}{\alpha x'}\left(\frac{x'}{\bar{h}_s}\right)^{\mathrm{i}\omega/\alpha}\delta\left(t'-T_0+\frac{1}{\alpha}\ln\frac{x'}{\bar{h}_s}\right)\right)$$
$$\times\delta\left(\bar{c}(t-t')-\frac{\alpha}{2\bar{c}}(x^2-x'^2)-|x-x'|\right)\left(\frac{\alpha x'}{\bar{c}}+\mathrm{sgn}(x-x')\right)\mathrm{d}x'.$$

Equation (B 2) describes the integral of the historical contribution of the entropy gradient at the mean shock position and can be rearranged to show that

$$
\begin{aligned}
Q_1(x,t) = &-\frac{\bar{T}\bar{c}}{2}\frac{1}{\alpha\bar{h}_s}\mathscr{S}l\frac{H(\bar{c}(t-T_0)-(\alpha/2\bar{c})(x^2-\bar{h}_s^2)-(\bar{h}_s-x))}{(1+\alpha(t-T_0))^{1/2}}\\
&-\frac{\bar{T}\bar{c}}{2}\frac{\mathrm{i}\omega}{\alpha\bar{h}_s}\mathscr{S}l\mathrm{e}^{-\mathrm{i}\omega T_0}\frac{x}{2\bar{c}}\int_1^{\sigma}\mathrm{d}q\,q^{-3/2}\\
&\times\exp\left[\mathrm{i}\omega\left(-\frac{q-1}{\alpha}+t-\frac{\alpha}{2\bar{c}^2}(x^2-\bar{h}_s^2)-\frac{1}{\bar{c}}(\bar{h}_s-x)\right)\right]\\
&-\frac{\bar{T}\bar{c}}{2}\frac{\mathrm{i}\omega}{\alpha\bar{h}_s}\mathscr{S}l\mathrm{e}^{-\mathrm{i}\omega T_0}\frac{1}{\alpha}\int_1^{\sigma}\mathrm{d}q\left(q^{-1/2}-\frac{\alpha\bar{h}_s}{2\bar{c}}q^{-3/2}\right)\\
&\times\exp\left[\mathrm{i}\omega\left(-\frac{q-1}{\alpha}+t-\frac{\alpha}{2\bar{c}^2}(x^2-\bar{h}_s^2)-\frac{1}{\bar{c}}(\bar{h}_s-x)\right)\right]
\end{aligned}
$$

where

$$
\sigma = 1+\alpha(t-T_0)-\frac{\alpha}{\bar{c}}(\bar{h}_s-x)-\frac{\alpha^2}{2\bar{c}^2}(x^2-\bar{h}_s^2).
$$

The last term in $Q_1(x,t)$ has the same argument, $t+x/\bar{c}-\frac{1}{2}\alpha x^2/\bar{c}^2$, as the downstream propagating free wave in (2.13) and, hence, can be incorporated into the yet to be determined function $P(t+x/\bar{c}-\frac{1}{2}\alpha x^2/\bar{c}^2)$ describing this travelling wave component. Similarly, the image term $Q_1(-x,t)$ contributes a corresponding term into the upstream propagating wave. The remaining integral in the non-propagating terms, $\tilde{Q}_1(x,t)$, can be expressed in terms of the incomplete Gamma function $\Gamma(a,b)$:

$$
\begin{aligned}
\tilde{Q}_1(x,t) = &-\frac{\bar{T}\bar{c}}{2}\frac{1}{\alpha\bar{h}_s}\mathscr{S}l\frac{H(\bar{c}(t-T_0)-(\alpha/2\bar{c})(x^2-\bar{h}_s^2)-(\bar{h}_s-x))}{(1+\alpha(t-T_0))^{1/2}}\\
&-\frac{\bar{T}x}{4}\frac{\mathrm{i}\omega}{\alpha\bar{h}_s}\mathscr{S}l\exp\left[\mathrm{i}\omega\left(t-T_0-\frac{\alpha}{2\bar{c}^2}(x^2-\bar{h}_s^2)-\frac{1}{\bar{c}}(\bar{h}_s-x)\right)\mathrm{e}^{\mathrm{i}\omega/\alpha}(\mathrm{i}\omega/\alpha)^{1/2}\right]\\
&\times\left(\Gamma\left(-\frac{1}{2},\frac{\mathrm{i}\omega}{\alpha}\right)-\Gamma\left(-\frac{1}{2},\frac{\mathrm{i}\omega}{\alpha}\left(1+\alpha(t-T_0)-\frac{\alpha}{\bar{c}}(\bar{h}_s-x)-\frac{\alpha^2}{2\bar{c}^2}(x^2-\bar{h}_s^2)\right)\right)\right),
\end{aligned}
\tag{B 4}
$$

where $\Gamma(a,b)=\int_b^{\infty}t^{a-1}\mathrm{e}^{-t}\,\mathrm{d}t$. The branch cut in (B 4) is chosen to be along the positive imaginary axis of ω in order to give roots symmetric about $\mathrm{Re}(\omega)=0$. Letting $t-T_0\to\infty$, the expression for $\tilde{Q}_1(x,t)$ in (B 4) simplifies to

$$
\begin{aligned}
\tilde{Q}_1(x,t) = &-\frac{\bar{T}x}{4}\frac{\mathrm{i}\omega}{\alpha\bar{h}_s}\mathscr{S}l\,\mathrm{e}^{\mathrm{i}\omega/\alpha}(\mathrm{i}\omega/\alpha)^{1/2}\Gamma\left(-\frac{1}{2},\frac{\mathrm{i}\omega}{\alpha}\right)\\
&\times\exp\left[\mathrm{i}\omega\left(t-T_0-\frac{\alpha}{2\bar{c}^2}(x^2-\bar{h}_s^2)-\frac{1}{\bar{c}}(\bar{h}_s-x)\right)\right]\\
&-\frac{\bar{T}\bar{c}}{2\alpha\bar{h}_s}\mathscr{S}l(\alpha(t-T_0))^{-1/2}+\frac{\bar{T}x}{4\bar{h}_s}\mathscr{S}l(\alpha(t-T_0))^{-3/2}.
\end{aligned}
\tag{B 5}
$$

The last two decaying terms are from the starting contribution at $t'=T_0$.

Evaluating the t' integral in (B 3) gives

$$Q_2(x,t) = \frac{\bar{T}}{2}\mathscr{S}l\mathrm{e}^{-\mathrm{i}\omega T_0}\int_0^{\bar{h}_s}\mathrm{d}x'\,\frac{(\alpha x'/\bar{c}+\mathrm{sgn}(x-x'))}{(1+(\alpha/\bar{c})(x-x'))^{1/2}}\exp\left[\mathrm{i}\omega\left(t-\frac{\alpha}{2\bar{c}^2}(x^2-x'^2)-\frac{1}{\bar{c}}|x-x'|\right)\right]$$
$$\times\left(\frac{\mathrm{i}\omega}{\alpha\bar{h}_s}\left(\frac{x'}{\bar{h}_s}\right)^{\mathrm{i}\omega/\alpha-1}H\left(t-T_0-\frac{\alpha}{2\bar{c}^2}(x^2-x'^2)-\frac{1}{\bar{c}}|x-x'|+\frac{1}{\alpha}\ln\frac{x'}{\bar{h}_s}\right)\right.$$
$$\left.+\frac{1}{\alpha x'}\left(\frac{x'}{\bar{h}_s}\right)^{\mathrm{i}\omega/\alpha}\delta\left(t-T_0-\frac{\alpha}{2\bar{c}^2}(x^2-x'^2)-\frac{1}{\bar{c}}|x-x'|+\frac{1}{\alpha}\ln\frac{x'}{\bar{h}_s}\right)\right). \tag{B 6}$$

To continue further we need to determine where the argument of the generalized functions H and δ vanishes, i.e. we have to find the position x_f of the front of the entropy-related fluctuations. x_f satisfies

$$t-T_0-\frac{\alpha}{2\bar{c}^2}(x^2-x_f^2)-\frac{1}{\bar{c}}|x-x_f|+\frac{1}{\alpha}\ln\frac{x_f}{\bar{h}_s}=0,$$

giving

$$x_f=\bar{h}_s\mathrm{e}^{-\alpha(t-T_0)}\left(1+\frac{\alpha x}{\bar{c}}-\frac{\alpha}{\bar{c}}\bar{h}_s\mathrm{e}^{-\alpha(t-T_0)}\right)+O(\bar{M}_2^2),$$

which decays exponentially as $t-T_0\to\infty$. Equation (B 6) can be rearranged to show that

$$Q_2(x,t)=\frac{\bar{T}}{2}\mathscr{S}l\mathrm{e}^{-\mathrm{i}\omega T_0}\int_{x_f}^{\bar{h}_s}\mathrm{d}x'\,\frac{\mathrm{sgn}(x-x')+\alpha x'/\bar{c}-(\alpha/2\bar{c})(x-x')}{1+(\alpha x'/\bar{c})\mathrm{sgn}(x-x')}$$
$$\times\frac{\partial}{\partial x'}\left(\left(\frac{x'}{\bar{h}_s}\right)^{\mathrm{i}\omega/\alpha}\exp\left[\mathrm{i}\omega\left(t-\frac{\alpha}{2\bar{c}^2}(x^2-x'^2)-\frac{1}{\bar{c}}|x-x'|\right)\right]\right)$$
$$+\frac{\bar{T}}{2}\mathscr{S}l\left(1-\frac{\alpha x}{2\bar{c}}+\frac{\alpha\bar{h}_s}{2\bar{c}}\mathrm{e}^{-\alpha(t-T_0)}\right)+O(\bar{M}_2^2). \tag{B 7}$$

Equation (B 7) can hence be integrated by parts to give

$$Q_2(x,t)=\frac{\bar{T}}{2}\mathscr{S}l\mathrm{e}^{-\mathrm{i}\omega T_0}\left(\exp\left[\mathrm{i}\omega\left(t-\frac{\alpha}{2\bar{c}^2}(x^2-\bar{h}_s^2)-\frac{1}{\bar{c}}(\bar{h}_s-x)\right)\right]\left(-1+\frac{\alpha\bar{h}_s}{2\bar{c}}-\frac{\alpha x}{2\bar{c}}\right)\right.$$
$$-\mathrm{e}^{-\mathrm{i}\omega(t-T_0)}\left(1+\mathrm{i}\frac{\omega x}{\bar{c}}\right)\exp\left[\mathrm{i}\omega\left(t-\frac{\alpha}{2\bar{c}^2}x^2-\frac{1}{\bar{c}}x\right)\right]\left(1-\frac{\alpha x}{2\bar{c}}\right)$$
$$\left.-\int_{x_f}^{\bar{h}_s}\mathrm{d}x'\left(\frac{x'}{\bar{h}_s}\right)^{\mathrm{i}\omega/\alpha}\exp\left[\mathrm{i}\omega\left(t-\frac{\alpha}{2\bar{c}^2}(x^2-x'^2)-\frac{1}{\bar{c}}|x-x'|\right)\right]\left(-2\delta(x-x')+\frac{\alpha}{2\bar{c}}\right)\right)$$
$$+\frac{\bar{T}}{2}\mathscr{S}l\left(1-\frac{\alpha x}{2\bar{c}}+\frac{\alpha\bar{h}_s}{2\bar{c}}\mathrm{e}^{-\alpha(t-T_0)}\right)+O(\bar{M}_2^2).$$

Incorporating the downstream propagating terms into the travelling component, we get

$$\tilde{Q}_2(x,t)=\bar{T}\mathscr{S}l\left(\frac{x}{\bar{h}_s}\right)^{\mathrm{i}\omega/\alpha}\mathrm{e}^{\mathrm{i}\omega(t-T_0)}-\frac{\bar{T}\alpha}{4\bar{c}}\mathscr{S}l\int_{x_f}^{\bar{h}_s}\mathrm{d}x'\left(\frac{x'}{\bar{h}_s}\right)^{\mathrm{i}\omega/\alpha}$$
$$\exp\left[\mathrm{i}\omega\left(t-T_0-\frac{\alpha}{2\bar{c}^2}(x^2-x'^2)-\frac{1}{\bar{c}}|x-x'|\right)\right]$$

$$-\frac{\bar{T}\alpha x}{4\bar{c}}\mathscr{S}l\exp\left[\mathrm{i}\omega\left(t-T_0-\frac{\alpha}{2\bar{c}^2}(x^2-\bar{h}_s^2)-\frac{1}{\bar{c}}(\bar{h}_s-x)\right)\right]$$

$$-\frac{\bar{T}}{2}\mathscr{S}l\left(1-\frac{\alpha x}{2\bar{c}}\right)\left(1+\frac{\mathrm{i}\omega x}{\bar{c}}\right)\exp\left[-\mathrm{i}\omega\left(\frac{\alpha x^2}{2\bar{c}^2}+\frac{x}{\bar{c}}\right)\right], \tag{B 8}$$

as $t-T_0\to\infty$. The first term is from the local entropy fluctuation and the second term is the summation of the entropy contribution in the stagnation flow region at the retarded time. The third and fourth terms are from contributions of entropy fluctuations at the mean shock position $\bar{h}_s$ and at the front x_f (≈ 0) respectively.

We can manipulate the image term $Q(-x,t)$ in the same way and incorporate the travelling wave component into the upstream propagating term. This gives the additional non-propagating components, say $\tilde{Q}(-x,t)$. Hence, the non-propagating terms of (2.13) induced by the entropy fluctuation are the summation of (B 5), (B 8) and $\tilde{Q}(-x,t)$ which is

$$\tilde{Q}_1(x,t)+\tilde{Q}_2(x,t)+\tilde{Q}(-x,t)=\bar{T}\mathscr{S}l\left(\frac{x'}{\bar{h}_s}\right)^{\mathrm{i}\omega/\alpha}\mathrm{e}^{\mathrm{i}\omega(t-T_0)}$$

$$-\frac{\bar{T}x}{4}\frac{\mathrm{i}\omega}{\alpha\bar{h}_s}\mathscr{S}l\left(\mathrm{e}^{\mathrm{i}\omega/\alpha}\left(\frac{\mathrm{i}\omega}{\alpha}\right)^{1/2}\Gamma\left(-\frac{1}{2},\frac{\mathrm{i}\omega}{\alpha}\right)\right)$$

$$\times\left(\exp\left[\mathrm{i}\omega\left(t-T_0-\frac{\alpha}{2\bar{c}^2}(x^2-\bar{h}_s^2)-\frac{1}{\bar{c}}(\bar{h}_s-x)\right)\right]\right.$$

$$\left.-\exp\left[\mathrm{i}\omega\left(t-T_0-\frac{\alpha}{2\bar{c}^2}(x^2-\bar{h}_s^2)-\frac{1}{\bar{c}}(\bar{h}_s+x)\right)\right]\right)$$

$$-\frac{\bar{T}\alpha x}{4\bar{c}}\mathscr{S}l\left(\exp\left[\mathrm{i}\omega\left(t-T_0-\frac{\alpha}{2\bar{c}^2}(x^2-\bar{h}_s^2)-\frac{1}{\bar{c}}(\bar{h}_s-x)\right)\right]\right.$$

$$\left.-\exp\left[\mathrm{i}\omega\left(t-T_0-\frac{\alpha}{2\bar{c}^2}(x^2-\bar{h}_s^2)-\frac{1}{\bar{c}}(\bar{h}_s+x)\right)\right]\right)$$

$$-\frac{\bar{T}\alpha}{4\bar{c}}\mathscr{S}l\int_{x_f}^{\bar{h}_s}\mathrm{d}x'\left(\frac{x'}{\bar{h}_s}\right)^{\mathrm{i}\omega/\alpha}\left(\exp\left[\mathrm{i}\omega\left(t-T_0-\frac{\alpha}{2\bar{c}^2}(x^2-x'^2)-\frac{1}{\bar{c}}|x-x'|\right)\right]\right.$$

$$\left.+\exp\left[\mathrm{i}\omega\left(t-T_0-\frac{\alpha}{2\bar{c}^2}(x^2-x'^2)-\frac{1}{\bar{c}}|x+x'|\right)\right]\right)$$

$$-\frac{\bar{T}\bar{c}}{\alpha\bar{h}_s}\mathscr{S}l(\alpha(t-T_0))^{-1/2}+\frac{\bar{T}\alpha\bar{h}_s}{2\bar{c}}\mathscr{S}l\mathrm{e}^{-\alpha(t-T_0)}$$

as $t-T_0\to\infty$. We are interested in oscillations of frequency ω and so the terms in the last line describing monotonically decaying transients can be discarded for large $t-T_0$.

Appendix C. Integration of volumetric entropy contribution

We aim to evaluate

$$-\frac{\bar{T}\alpha}{4\bar{c}}\mathscr{S}l\int_{x_f}^{\bar{h}_s}\mathrm{d}x'\left(\frac{x'}{\bar{h}_s}\right)^{\mathrm{i}\omega/\alpha}\left(\exp\left[\mathrm{i}\omega\left(t-T_0-\frac{\alpha}{2\bar{c}^2}(\bar{h}_s^2-x'^2)-\frac{1}{\bar{c}}(\bar{h}_s-x')\right)\right]\right.$$

$$\left.+\exp\left[\mathrm{i}\omega\left(t-T_0-\frac{\alpha}{2\bar{c}^2}(\bar{h}_s^2-x'^2)-\frac{1}{\bar{c}}(\bar{h}_s+x')\right)\right]\right)$$

which is equivalent to

$$-\frac{\bar{T}\alpha}{4\bar{c}}\mathscr{S}l\exp\left[\mathrm{i}\omega\left(t-T_0-\frac{\bar{h}_s}{\bar{c}}\right)\right]\int_{x_f}^{\bar{h}_s}\mathrm{d}x'\left(\frac{x'}{\bar{h}_s}\right)^{\mathrm{i}\omega/\alpha}\left(\mathrm{e}^{\mathrm{i}\omega x'/\bar{c}}+\mathrm{e}^{-\mathrm{i}\omega x'/\bar{c}}\right)+O(\bar{M}_2^2) \quad (C\,1)$$

where $x_f \approx \bar{h}_s\mathrm{e}^{-\alpha(t-T_0)}(1+\alpha\bar{h}_s/\bar{c})$.

Using the formula

$$\int_l^u y^a\mathrm{e}^{by}\,\mathrm{d}y = \sum_{j=1}^{n}\frac{(-1)^{j-1}b^{j-1}y^{a+j}\mathrm{e}^{by}}{(a+1)(a+2)\ldots(a+j)}\Big|_l^u+\frac{(-1)^n b^n}{(a+1)(a+2)\ldots(a+n)}\int_l^u y^{a+n}\mathrm{e}^{by}\,\mathrm{d}y,$$

we can carry out the integration in (C 1)

$$-\frac{\bar{T}\alpha\bar{h}_s}{4\bar{c}}\mathscr{S}l\exp\left[\mathrm{i}\omega\left(t-T_0-\frac{\bar{h}_s}{\bar{c}}\right)\right]\sum_{j=1}^{n}\frac{\mathrm{e}^{\mathrm{i}\omega\bar{h}_s/\bar{c}}(-\mathrm{i}\omega\bar{h}_s/\bar{c})^{(j-1)}+\mathrm{e}^{-\mathrm{i}\omega\bar{h}_s/\bar{c}}(\mathrm{i}\omega\bar{h}_s/\bar{c})^{(j-1)}}{(\mathrm{i}\omega/\alpha+1)(\mathrm{i}\omega/\alpha+2)\ldots(\mathrm{i}\omega/\alpha+j)}$$

$$-\frac{\bar{T}\alpha\bar{h}_s}{4\bar{c}}\mathscr{S}l\exp\left[\mathrm{i}\omega\left(t-T_0-\frac{\bar{h}_s}{\bar{c}}\right)\right]\frac{(-1)^n((\mathrm{i}\omega\bar{h}_s/\bar{c})^n+(-\mathrm{i}\omega\bar{h}_s/\bar{c})^n)}{(\mathrm{i}\omega/\alpha+1)(\mathrm{i}\omega/\alpha+2)\ldots(\mathrm{i}\omega/\alpha+n)}$$

$$\times\int_{x_f}^{\bar{h}_s}(x'/\bar{h}_s)^{\mathrm{i}\omega/\alpha+n}\mathrm{e}^{\mathrm{i}\omega/\bar{c}x'}\,\mathrm{d}\left(\frac{x'}{\bar{h}_s}\right)$$

$$+\frac{\bar{T}\alpha\bar{h}_s}{4\bar{c}}\mathscr{S}l\mathrm{e}^{-\mathrm{i}\omega\bar{h}_s/\bar{c}}\sum_{j=1}^{n}\frac{\mathrm{e}^{-\alpha(t-T_0)j}(1+\mathrm{i}\omega\bar{h}_s/\bar{c}+j\,\alpha\bar{h}_s/\bar{c})((-\mathrm{i}\omega\bar{h}_s/\bar{c})^{j-1}+(\mathrm{i}\omega\bar{h}_s/\bar{c})^{j-1})}{(\mathrm{i}\omega/\alpha+1)(\mathrm{i}\omega/\alpha+2)\ldots(\mathrm{i}\omega/\alpha+j)}.$$

Letting $n\to\infty$, the second term can be neglected and the last term can be truncated since $t-T_0\to\infty$.

Hence, the final result of the integral (C 1) is

$$-\frac{\bar{T}\alpha\bar{h}_s}{2\bar{c}}\mathscr{S}l\mathscr{D}(\omega)\exp\left[\mathrm{i}\omega\left(t-T_0-\frac{\bar{h}_s}{\bar{c}}\right)\right]$$

where

$$\mathscr{D}(\omega)=\frac{1}{2}\sum_{j=1}^{\infty}\frac{\mathrm{e}^{\mathrm{i}\omega\bar{h}_s/\bar{c}}(-\mathrm{i}\omega\bar{h}_s/\bar{c})^{(j-1)}+\mathrm{e}^{-\mathrm{i}\omega\bar{h}_s/\bar{c}}(\mathrm{i}\omega\bar{h}_s/\bar{c})^{(j-1)}}{(\mathrm{i}\omega/\alpha+1)(\mathrm{i}\omega/\alpha+2)\ldots(\mathrm{i}\omega/\alpha+j)}.$$

REFERENCES

CARLING, J. C. & HUNT, B. L. 1974 The near wall jet of a normally impinging uniform, axisymmetric supersonic jet. *J. Fluid Mech.* **66**, 159–176.

CHANAUD, R. C. & POWELL, A. 1963 Some experiments concerning the hole and ring tone. *J. Acoust. Soc. Am.* **37**, 901–911.

DENTON, J. D. 1993 VIB3D, method for calculating 3-D unsteady flow through turbomachinery blades. *Cambridge Univ. Eng. Dept. Tech. Rep.*

GLAZNEV, V. N. 1977 Sound field of an underexpanded supersonic jet impinging on a barrier. *Sov. Phys. Acoust.* **23**, 142–145.

GLAZNEV, V. N., DEMIN, V. S. & YAKUSHEV, A. M. 1977 Self-oscillations in an underexpanded jet flowing into a barrier. *Fluid Dyn. USSR.* **12**, 848–852.

GUMMER, J. H. & HUNT, B. L. 1971 The impingement of a uniform, axisymmetric, supersonic jet on a perpendicular flat plate. *Aeronaut. Q.* **22**, 403–420.

HARTMANN, J. 1939 The acoustic air-jet generator. Ingeniørvidenskabelige Skrifter, No. 4.

HARTMANN, J. & TROLLE, B. 1927 A new acoustic generator. The air-jet generator. *J. Sci. Instrum.* **4** 101–111.

HENDERSON, B. & POWELL, A. 1993 Experiments concerning tones produced by an axisymmetric choked jet impinging on flat plates. *J. Sound Vib.* **168**, 307–326.

HO, C. M. & NOSSEIR, N. S. 1981 Dynamics of an impinging jet. Part 1. The feedback phenomenon. *J. Fluid Mech.* **105**, 119–142.

HOWE, M. S. 1975 Contributions to the theory of aerodynamic sound, with application to excess jet noise and the theory of the flute. *J. Fluid Mech.* **71**, 625–673.

KALGHATGI, G. T. & HUNT, B. L. 1976 The occurrence of stagnation bubbles in supersonic jet impingement flows. *Aeronaut. Q.* **27**, 169–185.

MØRCH, K. A. 1963 Shock instability in the Hartmann air-jet generator. *Fluid Mech. Lab. Tech. Univ. Denmark.* LFM R 63-2.

MØRCH, K. A. 1964 A theory for the mode of operation of the Hartmann air jet generator. *J. Fluid Mech.* **20**, 141–159.

MØRCH, K. A. 1973 On the impingingement of a composite jet. *Tech. Univ. Denmark. DCAMM Rep.* 47.

POWELL, A. 1988 The sound-producing oscillations of round underexpanded jets impinging on normal plates. *J. Acoust. Soc. Am.* **83**, 515–533.

ROCKWELL, D. & NAUDASCHER, E. 1979 Self-sustained oscillations of impinging free shear layers. *Ann. Rev. Fluid Mech.* **11**, 67–94.

SHAPIRO, A. H. 1954 *The Dynamics and Thermodynamics of Compressible Fluid Flow*, vol II. The Ronald Press Company, New York.

TAM, C. K. W. & AHUJA, K. K. 1990 Theoretical model of discrete tone generation by impinging jets. *J. Fluid Mech.* **214**, 67–87.

TAYLOR, K. 1978 A transformation of the acoustic equation with implications for wind-tunnel and low-speed flight tests. *Proc. R. Soc. Lond.* A **363**, 271–281.